



# Au NPs-incorporated NiS/RGO hybrid composites for efficient visible light photocatalytic hydrogen evolution

P. Senthil<sup>1,4</sup>, A. Sankar<sup>1,\*</sup> , K. Paramasivaganesh<sup>2</sup>, and S. P. Saravanan<sup>3</sup>

<sup>1</sup> Department of Chemistry, Kandaswami Kandar's College, P. Velur, Namakkal, Tamilnadu 638182, India

<sup>2</sup> Department of Chemistry, Arumugam Pillai Seethai Ammal College, Thiruppathur, Sivagangai, Tamilnadu 630211, India

<sup>3</sup> Department of Chemistry, Karuppanan Mariappan College, Chettiarpalayam, Muthur, Tamilnadu 638105, India

<sup>4</sup> Department of Chemistry, Mahendra Institute of Technology, Mallasamudram (W), Namakkal, Tamilnadu 637503, India

**Received:** 10 July 2023

**Accepted:** 22 November 2023

**Published online:**  
18 December 2023

© The Author(s), under exclusive licence to Springer Science+Business Media, LLC, part of Springer Nature, 2023

## ABSTRACT

Hydrogen evolution reaction (HER) through electrocatalytic water splitting is regarded as a promising route to produce hydrogen in a large scale. Designing a low-cost, large-scale, and highly active electrolytic hydrogen production catalyst is still a huge challenge. Incorporation of high-loading redox-active materials with small amounts of graphene is a general protocol to achieve high-performance catalysts. Herein, reduced graphene oxide (RGO) and Au NPs cocatalysts-modified NiS hybrid composite photocatalysts were successfully synthesized via a facile hydrothermal method for hydrogen evolution reaction (HER). XRD results suggest the NiS with rhombohedral phase (# JCPDS No. 65-2117). Both SEM and TEM results reveal that Au with NiS sample has clear spherical-shaped nanoparticles sizes in the range of 30–40 nm are coated on the rGO nanosheets. The estimated optical band gap energy is in the order of Au NPs/NiS@rGO (2.36 eV) < NiS@rGO (2.67 eV) < pure NiS (2.91 eV). The surface areas of NiS, NiS@rGO, and Au-NiS@rGO were calculated to be 64.58, 87.6, and 106.35 m<sup>2</sup>g<sup>-1</sup>, respectively. The Au-NiS@rGO exhibits significantly enhanced catalytic activity for hydrogen evolution reaction (HER) in both the acid and alkaline electrolytes in comparison with the pristine NiS. The Au-NiS@rGO delivers a striking catalytic kinetic metrics of a small Tafel slope of 54 mV dec<sup>-1</sup>, a low overpotential of 252 mV at a current density of 10 mA cm<sup>-2</sup>, and long operation stability of 4 day in the acid electrolyte. The improved HER activity of the Au-NiS@rGO hybrid composite catalyst is attributed to the synergistic effect of the surface plasmon resonance of Au NPs and enhanced electron transfer on RGO. This work could offer a facile and low-cost strategy for the construction of composite photocatalysts with high-efficiency hydrogen generation activity.

Address correspondence to E-mail: sanvishnu2010@gmail.com

## 1 Introduction

Global warming and environmental deteriorating as a universal issue has tremendously motivated many researchers to focus on the renewable and clean energy sources. Hydrogen generation and storage [1] is one of the most promising solutions to resolve this issue. Hydrogen as a clean, safe, reproducible, and sustainable source has attracted many attentions in various fields of hydrogen storage as fuel cells and hydrogen evolution reaction [2, 3]. Although electrochemical splitting of water or electrolysis is a mature technology to generate high-purity hydrogen on a large scale to satisfy the future global energy demands [4, 5], the utilization of expensive Pt, the most efficient electrocatalyst for hydrogen evolution reaction (HER) with a near-zero onset potential benefited from a minimum free-energy change for the hydrogen adsorption on its surfaces, has largely curtailed the practical deployment of electrolysis for the massive production of hydrogen in energy utility sectors as the clean energy carrier due to its high cost. Therefore, it is imperative to develop non-precious electrocatalysts toward cost-effective hydrogen production. Among all, H<sub>2</sub> production via photocatalytic water splitting by semiconductors such as TiO<sub>2</sub>, WO<sub>3</sub>, ZnO, etc. is the most economical, simplest, and clean method [6–8]. This production of H<sub>2</sub> by photocatalytic water splitting has become an emerging area of research interest with great potential due to the global demand for alternative energy and environmental remediation [9, 10]. Further, one of the serious hurdles faced by most of the photocatalysts is the high electron–hole recombination rate, which leads to a low solar-to-hydrogen conversion efficiency [11]. Various approaches are adopted to solve this problem; for example, the conductive carbon materials such as graphene are combined with photocatalysts to prevent the photo-induced electron–hole pairs from recombination [12]. On the other hand, the combination of the photocatalyst with noble metal nanostructures has received much attention due to their surface plasmon resonance (SPR) properties. It has been well proved that the SPR effect not only improves the optical absorption of dyes but also enhances electron–hole formation in the photocatalysts [13–16].

Nickel sulfide (NiS) exhibits a strong tendency to form complex coordination. The electron density on nickel increases by the donating electrons of sulfide (S<sub>2</sub><sup>−</sup>) to nickel metal atoms, which makes the NiS

readily available to identically suitable moieties to interact and form a complex. In the view of this, NiS is being used as an active catalyst material for the HER activity due to its electronic interaction and abundant redox centers. Moreover, NiS has n-type narrow band gap (0.3–0.5 eV), responds to both visible and infrared light, and has attracted widespread attention as a co-catalyst [17]. However, pristine NiS associates with the instability during electrochemical reactions due to the changes in volume and electronic conductivity [18]. To achieve an efficient photocatalyst, combining NiS with carbon-based materials, such as graphene, is an effective means, and this has been immensely deployed in various energy conversion applications. The unique properties of graphene can facilitate the migration of photogenerated electrons to the active site, which can minimize the recombination of charge carriers and promote photocatalytic hydrogen generation. Owing to the stability issue, reduced graphene oxide (rGO) is being employed as an effective supporting material which stabilizes the redox reactions of NiS. Indeed, the hydrogen evolution efficient of NiS can be synergistically enhanced by introducing another component as cocatalysts to form NiS/rGO hybrid composite. Nickel sulfide (NiS) as a good alternative co-catalyst is cheap and can replace Pt in photocatalytic water splitting system [19, 20]. Au NPs as co-catalyst shows higher hydrogen evolution activity than those of noble metals in photocatalytic hydrogen evolution. Therefore, it can be speculated that combining NiS with rGO and Au NPs may provide a feasible approach to deal with the drawbacks of low efficiency and poor photo-stability simultaneously, which has remained unavailable so far. In this study, we have synthesized the highly active and stable photocatalyst for HER through facile hydrothermal route. Firstly, the Au nanoparticles (Au NP), which display the SPR at wavelengths of 400 nm, are anchored onto the rGO surface. Secondly, the noble metal Au, on the other hand, contributes to the activity by forming a Schottky barrier at the metal – semiconductor interface. This Schottky barrier can serve as an effective electron trap causing high density of states at the Fermi level (EF) of the interface and minimizing the charge carrier recombination. This electronic factor contributes to charge separation and utilization. Finally, the rGO-based support, due to the presence of an sp<sup>2</sup>-hybridized hexagonal carbon network, can transport electrons rapidly across its two-dimensional (2D) network to the active site of hydrogen generation, thus enhancing charge

utilization toward increasing the efficiency of photocatalysts. Then, the resulting composite serves as the substrate to load highly active NiS to form Au-NiS@rGO hybrid composite. To the best knowledge, it is the first time to investigate the Au-NiS@rGO hybrid composite for hydrogen evolution. HER performance of the Au-NiS@rGO catalyst was systematically investigated. The Au NPs show a higher catalytic activity than the pristine NiS nanocrystals in both acid and alkaline solutions. Our work expands the bimetallic sulfide family as efficient HER catalysts.

## 2 Experimental section

### 2.1 Materials and chemicals

Nickel nitrate ( $\text{Ni}(\text{NO}_3)_2 \cdot 6\text{H}_2\text{O}$ , Purity = 99.99%), Natural graphite powder (Purity = 99.99%; average particle size = 45  $\mu\text{m}$ ), Gold nitrate, ( $\text{AuNO}_3$ ), and thiourea ( $\text{CH}_4\text{N}_2\text{S}$ , Purity = 99.99%), were purchased from Sigma-Aldrich. Potassium permanganate ( $\text{KMnO}_4$ ), sodium nitrate ( $\text{NaNO}_3$ ), potassium hexacyanoferrate ( $\text{K}_4\text{Fe}(\text{CN})_6 \cdot 3\text{H}_2\text{O}$ ), Sulfuric acid (98%), hydrochloric acid, and hydrogen peroxide (30%) are analytical grade and procured from Merck Specialties Private Limited, India and used without further purification. All the aqueous solutions were prepared by using Milli-Q water, which were used during the experiments.

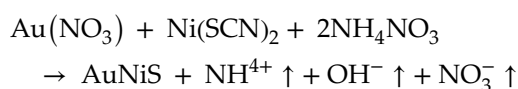
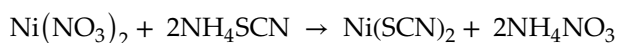
### 2.2 Synthesis of GO

Typically, flake graphite (10 g),  $\text{KMnO}_4$  (6 g), and  $\text{K}_2\text{FeO}_4$  (4 g) as the oxidants, and boric acid (0.01 g) as a stabilizer were first dispersed in 100 mL of concentrated sulfuric acid in a vessel and stirred for 1.5 h at less than 5 °C. After the addition of another  $\text{KMnO}_4$  (5 g), the vessel was transferred into a water bath at about 35 °C and stirred for another 3 h to complete the deep oxidation. Next, as 250 mL of deionized water was slowly added, the temperature was adjusted to 95 °C and held for 15 min, when the diluted suspension turned brown, indicating the hydrolysis and absolute exfoliation of intercalated graphite oxide. Finally, this brown suspension was further treated with 12 mL  $\text{H}_2\text{O}_2$  (30%) to reduce the residual oxidants and intermediates to soluble sulfate, then centrifuged at 10,000 rpm for 20 min to remove

the residual graphite, and washed with 1 mol/L HCl and deionized water repeatedly, producing the terminal GO.

### 2.3 Synthesis of Au/NiS@rGO

First, 2D rGO was prepared via the modified Hummers' method [21]. The nanocomposite Au/NiS@rGO (0.5:1:1 w/w) was synthesized by adopting the eco-friendly hydrothermal method using thiourea as an oxidizing agent in alkaline medium. It is to be noted that no surfactant molecules are added in the preparation to retain the metallic nanoparticle, and this makes the procedure simple. In a typical procedure, 0.5 g of rGO was well dispersed in 50 mL of water by sonication. Then, 50 mL of aqueous solutions of metal precursors  $\text{AuNO}_3$  (0.04 g) and  $\text{Ni}(\text{NO}_3)_2$  (0.06 g) were added, while maintaining the molar ratio of Au-Ni (0.2:1). Subsequently, 10 mL thiourea solutions (contained 75 mg  $\text{CH}_4\text{N}_2\text{S}$ ) were added above the mixed solution and stirred for 20 min. Then, the whole mixture was stirred vigorously for 2 h at room temperature and transferred into an autoclave. The autoclave was put into a furnace at 180 °C for 12 h and allowed to cool to room temperature. The product was separated by centrifugation, washed with distilled water and absolute ethanol several times to remove impurities, and dried in a vacuum oven at 45 °C. Lastly, the composite multidimensional photocatalyst of Au/NiS@rGO was obtained. Finally, Au/NiS@rGO, which the quality scores of Au was 5 wt%, was synthesized. The same procedure was employed to synthesize the NiS nanoparticles without the use of  $\text{AuNO}_3$  and rGO. The schematic representation of the synthesis process is shown in Figure S1. The synthesis reaction equation is as follows:



### 2.4 Characterization

The phase constitution of the photocatalysts was characterized by X-ray diffraction (XRD) (D2 phaser BRUKER,  $\text{Cu-K}\alpha = 0.15418 \text{ nm}$ ). The morphologies and microstructure of the sample were examined

using scanning electron microscopy (JEOL JSM-7000F, JAPAN), Transmission electron microscopy (TEM), and high-resolution transmission electron microscopy (HRTEM) (TEM, Philips, Tecnai 20). The UV absorption spectra of the sample were performed on a UV–Vis spectrophotometer (Shimadzu UV 3600, Japan). The chemical analysis was performed on a X-ray Photoelectron Spectrometer (XPS, Thermo KAlpha Spectrometer) using Al-Ka X-rays, 1486.6 eV). The Raman spectra were obtained using (JobineYvon, HR800) at room temperature in an ambient air. Electrochemical measurements were performed with a standard three-electrode setup (The Multi Autolab PGSTAT204).

## 2.5 Electrochemical measurements

The electrocatalytic hydrogen evolution activity of Au-NiS@rGO nanocomposites was measured by a three-electrode system. The reference electrode was Ag/AgCl electrode. The platinum electrode with an area of 1 cm × 1 cm was used as the counter electrode. The 0.5 mol/L H<sub>2</sub>SO<sub>4</sub> aqueous solution was used as the electrolyte. The preparation method of working electrode is as follows: Au-NiS@rGO powder was dispersed in a 1 mL solution consisting of 242.5 μL deionized water, 727.5 μL ethanol, and 30 μL 5 wt% Nafion. Then, after 30 min of ultrasound, a uniform suspension was formed and slowly dripped onto the 0.159 mg cm<sup>-2</sup> glassy carbon electrode. After natural drying, the Au-NiS@rGO working electrode was obtained. Electricity chemistry workstation (Zennium Pro) on properties of Au-NiS@rGO was analyzed. By linear sweep voltammetry scanning (LSV) (scanning rate is 5 mV/s), the linear scanning curve of catalyst hydrogen evolution process was measured. The curves of the overpotential and the log current density were plotted to obtain the Tafel curves for evaluating the kinetic properties of the catalyst. The electrode material was tested by electrochemical impedance spectroscopy (EIS), and the frequency range was 0.1–100 kHz.

## 3 Results and discussion

### 3.1 Structural analysis

The purity, crystallinity, and the phase formation of the prepared products synthesized are determined by XRD as shown in Fig. 1. The XRD pattern

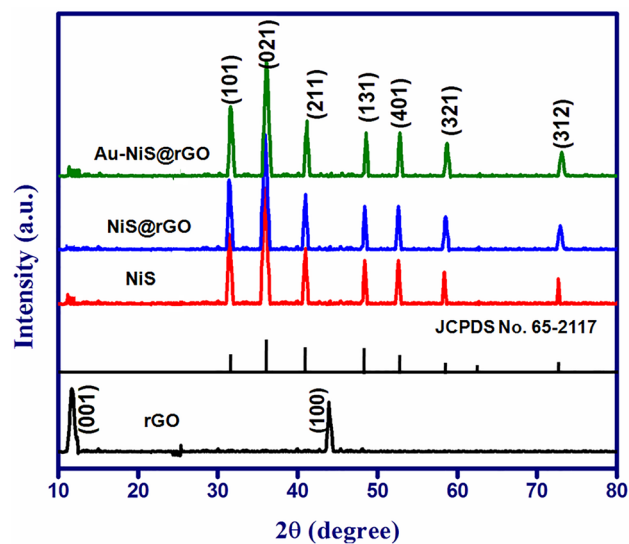


**Fig. 1** Powder XRD pattern of the samples

of wrinkled rGO nanosheets distinguishable by two identical peaks appearing at 10.41° and 42.31° associated with (001) and (111) confirms its presence [22]. All the primary diffraction peaks located at  $2\theta = 30.06^\circ$ ,  $35.38^\circ$ ,  $40.21^\circ$ ,  $48.65^\circ$ ,  $52.56^\circ$ ,  $57.15^\circ$ , and  $72.39^\circ$  correspond to the miller indices related to the planes (101), (021), (211), (131), (401), (321), and (312), which are matched for NiS with rhombohedral phase (# JCPDS No. 65-2117). There is no nickel oxide or hydroxide characteristic peaks detected, depicting the purity of the material. As presented in the XRD pattern of NiS/rGO composite in which the hydrothermal reduction process of GO started to anchor on NiS, the diffraction peaks of rGO diminished due to hydrophobic characteristics; however, the rGO network supports attractive electron transfer in the composite. These results were further supported by the SEM characterization and indicated that rGO could assist the growth of NiS because of the confirming function of rGO [23]. The average grain size was calculated from Debye Scherrer's formula.

$$d = \frac{K\lambda}{\beta \cos \theta}$$

where  $d$  is the mean crystallite size,  $K$  is the shape factor taken as 0.89,  $\lambda$  is the wavelength of the incident beam,  $\beta$  is the full width at half maximum, and  $\theta$  is the Bragg angle. The average crystalline size was found as 25 nm and 19 nm for NiS and Au/NiS@rGO composite samples, respectively. Williamson–Hall plots have

been further provided to identify the crystalline size, and the resultant plot of NiS and Au/NiS@rGO composite sample is shown in Figure S2 and S3. The slope and intercept value of the line fitted to the data points correspond to the strain value and average crystallite size, respectively. The values are 28 nm 20 nm for NiS and Au/NiS@rGO composite sample, respectively. These results are good agreement with the crystalline size calculated from Debye formula.

### 3.2 Morphological analysis

The morphologies of the formed Au-NiS@rGO and NiS are characterized with SEM as depicted in Fig. 2. From Fig. 2a, the clear sheet like morphology of rGO was identified. We can clearly see that a large amount of NiS nanoparticles and Au NPs are attached to the pleated rGO surface from a typical SEM image of Au-NiS@rGO (Fig. 2b) and also it is difficult to distinguish them from each other. This happens due to the following proposed mechanism: (i) initially, NiS crystallizes into nanoparticles and (ii) the oxygen-containing groups and defects of rGO can serve as the nucleation sites for NiS sheets, inhibiting them from growing into a spherical like nanoparticles. It can be found that Au/NiO NPs are embedded into the rGO sheets to form a good contact, which is beneficial to the catalytic reaction. Furthermore, the lattice interplanar spacing with an interplanar distance is about 0.335 and 0.36 nm, corresponding to the (101) and (211) plane of rhombohedral phase (JCPDS No. 65-2117). The crystallites have lattice fringes of 0.29 nm, which is ascribed

to the (101) plane of NiS (JCPDS JCPDS No. 65-2117) (Fig. 2e). Moreover, the corresponding SAED pattern (inset Fig. 2e) showed bright dot spots and the estimated miller indices are in good agreement with the XRD results. The elemental mapping results suggest that the uniform distribution of Au, C, S, and Ni can be observed (Fig. 2f–i). This condition further confirms the successful doping of AuNPs and NiS nanoparticles on the rGO surface, and the product is quite pure. The Au, S, and Ni elements exhibit continuous and uniform distribution in rGO, indicating that Au/NiS NPs are homogeneously dispersed in rGO sheets. Moreover, the obtained atomic ratio of Au (5.5%), Ni (65.8%), S (25.2%), and C (4.5%) is 0.1:1:1:0.5. This ratio is matched well with the initial concentration, which is used in the experimental process.

### 3.3 Raman spectra analysis

The Raman spectra of GO and AuNPs-NiS@rGO are shown in Fig. 3a. Notably, Raman spectroscopy is an effective method for characterizing the structure of graphene substrate materials. Therefore, we further studied the existence of rGO in AuNPs-NiS nanocomposites by Raman spectroscopy in Fig. 3a. As reported in other studies, the D peak is mainly caused by the breathing-mode vibration of sp<sup>3</sup> carbon, which is generally considered the disordered vibration peak of graphene, which is used to characterize the structural defects or edges in graphene samples. This peak occurs at near 1352 cm<sup>-1</sup>. The G peak is considered the characteristic peak caused by the in-plane vibration of the

**Fig. 2** SEM images of **a** rGO; **b** Au/NiS@rGO; TEM image of **c** rGO; **d** Au/NiS@rGO; **e** HRTEM of Au/NiS@rGO; EDS mapping of **f** Au; **g** C; **h** S and **i** Ni

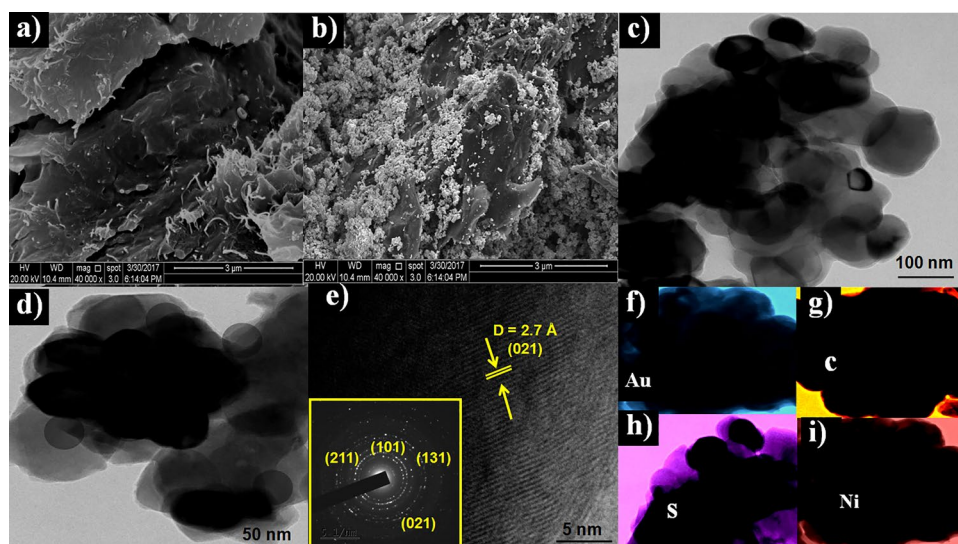
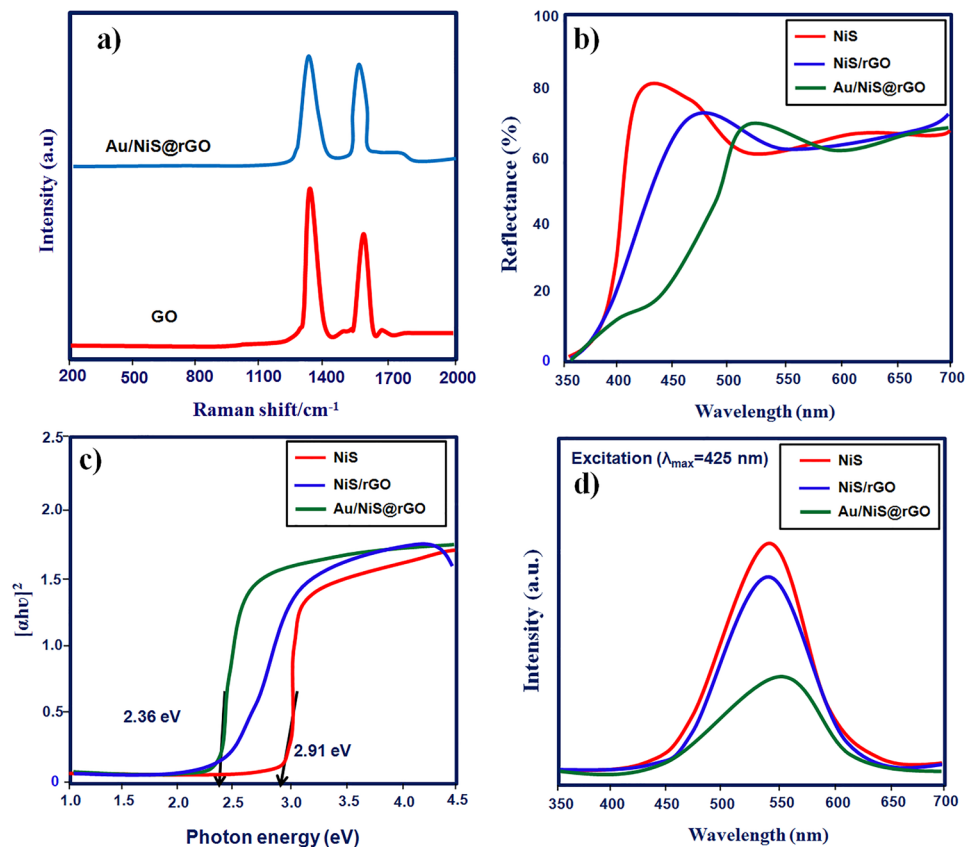


**Fig. 3** **a** Raman spectra, **b** UV absorption spectra and **b**  $K$ – $M$  plot of the prepared samples; **c** PL spectra of NiS, NiS@rGO and Au–NiS@rGO



sp<sup>2</sup> hybrid carbon atom, which occurs near 1584 cm<sup>-1</sup> [24, 25]. The degree of graphitization can be expressed by the strength ratio of D and G bands. Although the Raman spectra of all samples showed G and D peaks, they had some significant differences. Compared with the GO prepared under the same experimental conditions, the intensity ratio of the D band and the G band ( $I_D/I_G$ ) of the AuNPs–NiS/rGO is significantly increased, whereas the  $I_D/I_G$  reflects the defect density of graphene materials. The increase of  $I_D/I_G$  ratio in Au/NiS@rGO composite is due to the defects of GO increase with the reduction of oxygen-containing functional groups and GO is transformed into rGO. In addition, the increase in  $I_D/I_G$  indicates the successful GO reduction in the AuNPs–NiS/rGO nanocomposite.  $I_D/I_G$  ratio of the AuNPs–NiS/rGO nanocomposite is indicative of its excellent GO reduction.

### 3.4 Optical properties

To explore the optical absorption ability and recombination property of electrons and holes in the three samples, UV–vis DRS and PL emission spectra were used to analyze the optical properties. In Fig. 3b, all

three samples clearly show optical absorption under visible light. The  $E_g$  values estimated from Fig. 3c show the order of Au NPs/NiS@rGO (2.36 eV) < NiS@rGO (2.67 eV) < pure NiS (2.91 eV) (Fig. 3c). Thus, it is seen that the band gap of Au NPs/NiS@rGO is more positive than 1.23 eV (decomposition voltage of water) and in the range of the ideal band gap of 1.8–2.4 eV. The composite photocatalysts Au NPs/NiS@rGO display stronger broad background absorption in the region of 600–800 nm because of the narrow band of NiS [26, 27] and the SPR effect of Au [28]. A considerable red shift and narrowing the band gap energy are due to Au nanoparticles (Au NP), which display the SPR at wavelengths of 400 nm, and are anchored onto the rGO surface. In addition, the noble metal Au, on the other hand, contributes to the activity by forming a Schottky barrier at the metal – semiconductor interface. Then the intimate contact of rGO, Au, and NiS could make for the vectorial migrate of charge carriers among the components, enhancing the photogenerated carriers separation and the photocatalytic efficiency. The charge carrier trapping, transfer, and separation could be investigated with the photoluminescence (PL) emission spectra, which could help understanding the fate

of photo-induced electrons and holes in semiconductor. PL spectra in Fig. 3d give the similar trend that the peak of NiS at 550 nm is higher than Au NPs/NiS@rGO at 545 nm. The peak at around 500–550 nm is due to the surface defects and can form the exciton energy level near the bottom of the conduction band, which allows them to act as trapping sites and hinders the recombination of photogenerated charges. Moreover, the PL peaks of NiS and NiS@rGO exhibit almost unchanged position compared with the counterparts before combination with rGO, but decrease remarkably in intensity. The phenomenon displays that the recombination of photoexcited holes and electrons is well inhibited. Further introduction of Au to the heterostructures makes the PL peak of Au NPs/NiS@rGO drastically quenched, whose absorption is enhanced during the whole visible light range in line with the result given by the UV–vis diffuse reflectance spectra above. The observation reasonably suggests that noble metal Au and rGO cooperate to effectively suppress photogenerated electron–hole recombination [29].

### 3.5 Surface area analysis

The effectiveness of the electrocatalyst of the electrode materials for the HER depends heavily on their large specific surface area and pore size. Therefore,  $N_2$  adsorption–desorption was carried out to measure the samples' effective surface areas. NiS, NiS@rGO, and Au-NiS@rGO all exhibit a type-IV isotherm for  $N_2$  adsorption/desorption (Fig. 4a), indicating the existence of a mesoporous architecture [30–32]. Using the Brunauer–Emmett–Teller (BET) model, the surface areas of NiS, NiS@rGO, and Au-NiS@rGO were determined to be 64.58, 87.6, and 106.35  $m^2g^{-1}$ , respectively. According to the Barrett–Joyner–Halenda technique, the average pore width of NiS is 7.2 nm and that of Au-NiS@rGO is 14.2 nm (Fig. 4b). The results demonstrate that the surface area is dramatically enhanced by the creation of the Au-NiS@rGO composites, which significantly encourages adsorption and, in turn, boosts the HER activity.

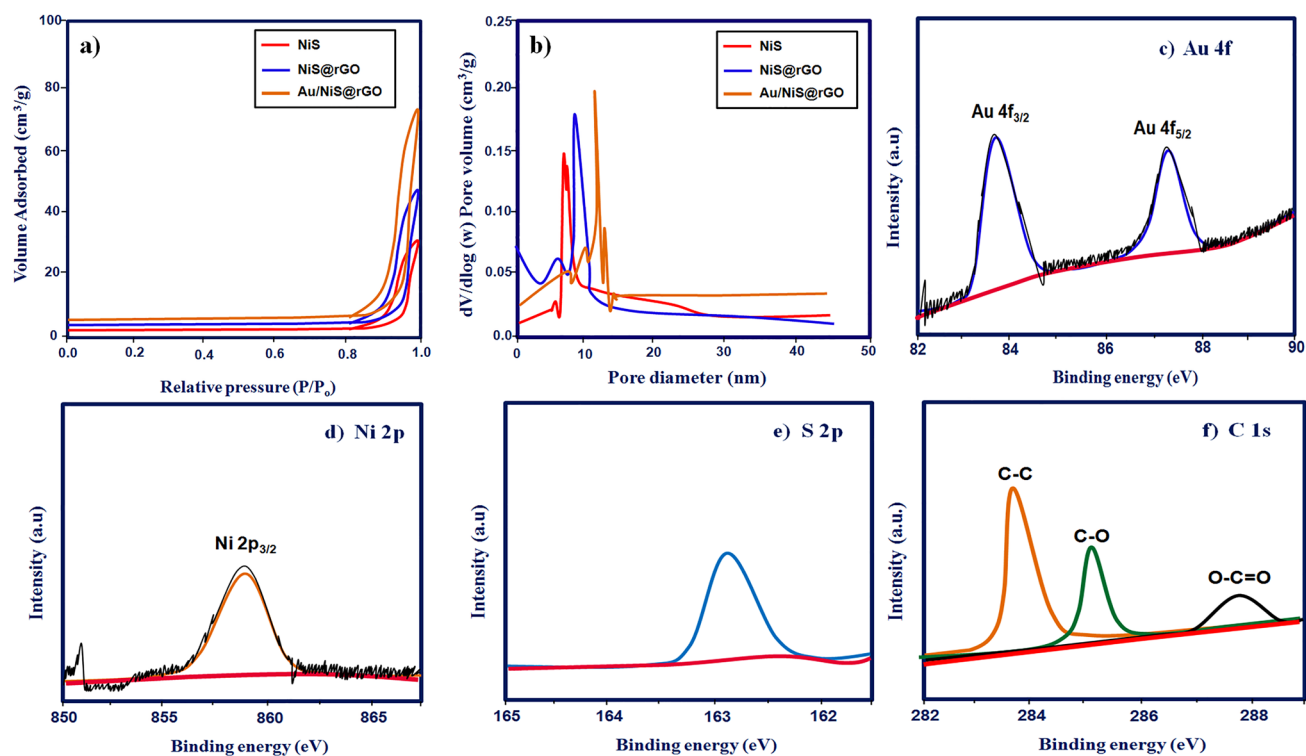


**Fig. 4** **a**  $N_2$  adsorption–desorption spectra and **b** pore size distribution of NiS, NiS@rGO and Au-NiS@rGO samples; high-resolution XPS spectra of **c** Au 4f; **d** Ni 2p; **e** S 2p and **f** C 1s

### 3.6 XPS analysis

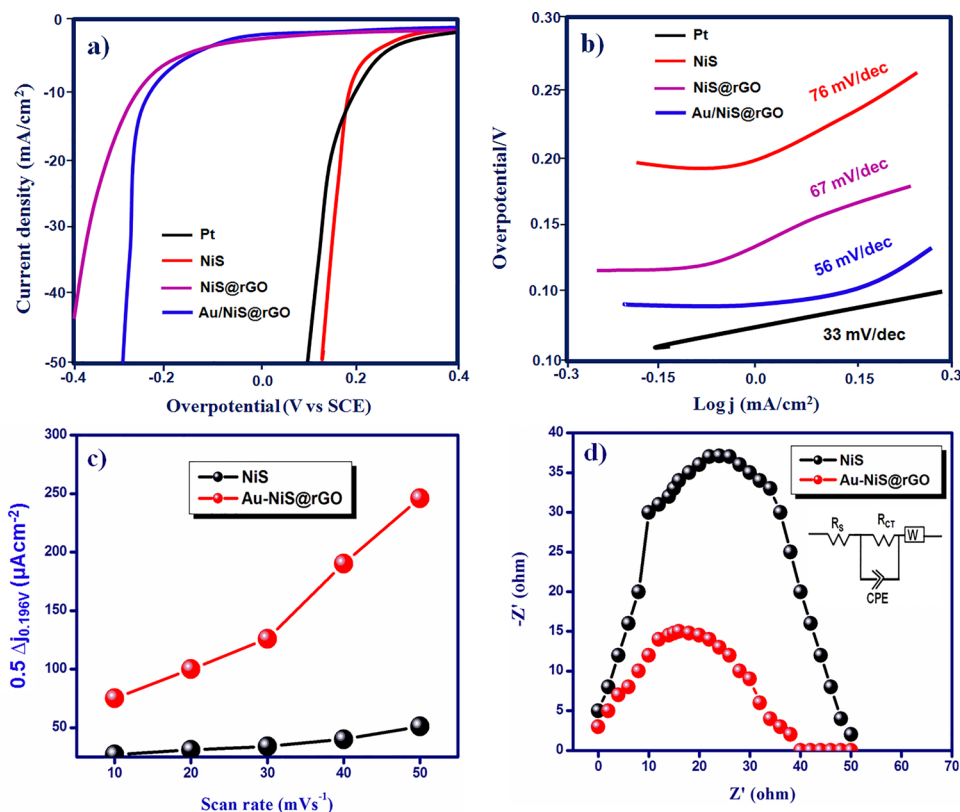
The elemental and valence state analysis provided by the XPS was used to corroborate the effective synthesis of Au-NiS@rGO composites. The two peaks at 83.9 eV and 87.57 eV, which represent Au 4f<sub>7/2</sub> and Au 4f<sub>5/2</sub> of Au<sup>0</sup> [33] (Fig. 4c), verified the existence of Au NPs in the composite. One minor peak at 858.5 eV (Fig. 4d) and one significant peak at 163.3 eV (Fig. 4e) in the Ni 2p and S 2p spectral were very close to the stated values for NiS [34]. The C 1s core-level spectrum is depicted in Fig. 4f, and it exhibits three peaks at 284.7, 285.7, and 288.5 eV that can be ascribed to rGO using functioning group analysis [35].

### 3.7 Electrocatalytic activity

In a 0.5 M H<sub>2</sub>SO<sub>4</sub> electrolyte with a graphite rod as the counter electrode, the performance of HER of Au-NiS@rGO and pure NiS was studied. The two samples' corrected curves of polar for iR are displayed in Fig. 5a. The HER metrics of Au-NiS@rGO are superior to those of pure NiS, with the former showing a lower onset potential for 187 mV at a current density of 1 mA cm<sup>-2</sup> and the latter having a faster increase in

cathodic currents at more negative potential. At a current density of 10 mAcm<sup>-2</sup>, the Au-NiS@rGO exhibits a little overpotential ( $\eta$ ) of 245 mV. The NiS has a value of 342 mV, thus this is lower. Au-NiS@rGO provides a cathodic current density of 34.98 mAcm<sup>-2</sup> at an overpotential of 30 mV, which is an increase of tenfold over the NiS sample's value (3.41 mAcm<sup>-2</sup>). Tafel plots for the two samples are shown together in Fig. 5b. For Au-NiS@rGO, the Tafel slope is predicted to be 56 mVdec<sup>-1</sup>, while for bare NiS, it is predicted to be 77 mVdec<sup>-1</sup>. Since a steeper Tafel slope indicates slower HER dynamics and lower activity, a smaller value for Au-NiS@rGO is recommended. With a Tafel slope of 55 mV dec-1, we can infer that the Volmer reaction is the rate-determining step in the HER process on Au-NiS@rGO (H<sup>+</sup> + e<sup>-</sup> → H\*; H\* + e<sup>-</sup> + H\* → H<sub>2</sub>). Tafel plots can be extrapolated to determine the exchange current density ( $j_0$ ), which is 0.66 mAcm<sup>-2</sup> for the Au-NiS@rGO and 0.27 mAcm<sup>-2</sup> for pure NiS. In addition, the HER performance of a commercial Pt/C catalyst was evaluated, and it was found to have a tiny Tafel slope of 31 mVdec<sup>-1</sup> and a low overpotential of 29 mV at a current density of 10 mAcm<sup>-2</sup>. Figure 5c depicts the current density as a function of scanning rate, and linear relationships can be used to describe these

**Fig. 5** Electrochemical HER performance in the 0.5 M H<sub>2</sub>SO<sub>4</sub>. **a, b** Polarization curves and corresponding Tafel plots of the Au/NiS@rGO, the NiS, and the commercial Pt/C. **c, d** Cdl and EIS measurements of the Au/NiS@rGO and the NiS

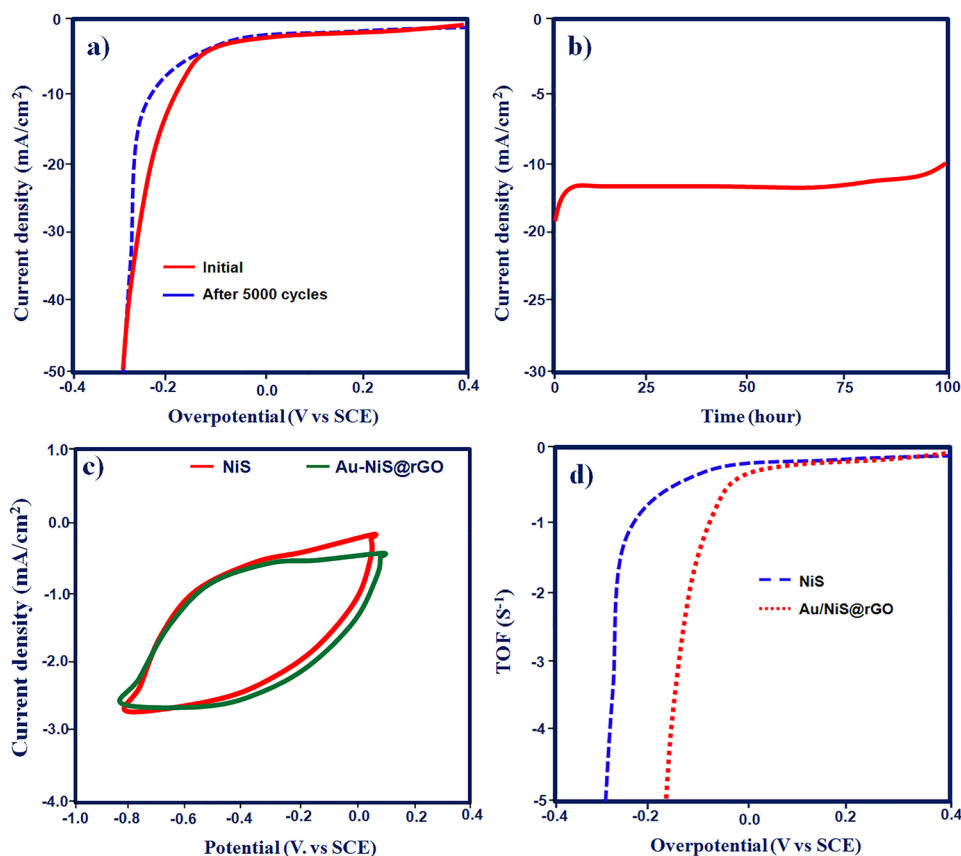




variations. For Au-NiS@rGO, the  $C_{dl}$  is determined to be  $4.4981 \text{ mFcm}^{-2}$ . In comparison to NiS, Au-NiS@rGO possesses a substantially greater ECSA, which is responsible for its superior HER efficacy (value  $\geq 0.639 \text{ mFcm}^{-2}$ ). Measurements of electrochemical impedance spectroscopy (EIS) were additionally performed at an overpotential of 345 mV vs. RHE to probe the charge transfer kinetics. Nyquist plots are shown in a semi-circular form in Fig. 5d. The charge transfer resistance ( $R_{ct}$ ) of Au-NiS@rGO is just 14.2, which is significantly lower than NiS's value ( $37.3\Omega$ ). This finding suggests that the conductive rGO nanosheets contribute to the Au-NiS@rGO's quicker charge transfer kinetics. The improved HER performance can be attributed to the Au-NiS@rGO's bigger ECSA and decreased charge transfer resistance compared to the NiS. The  $\text{H}_2\text{SO}_4$  electrolyte's effect on the Au-NiS@rGO catalyst's stability was studied. The Au-NiS@rGO LSV curves shown in Fig. 6a are almost identical to the first one after 5000 cycles, with a tiny negative shift of 14 mV at  $100 \text{ mAcm}^{-2}$ . At an overpotential of 260 mV vs. RHE, Fig. 6b depicts the time-dependent current density curve of the Au-NiS@rGO. Hydrogen evolution in

the Au-NiS@rGO has been seen to persist for 5 days without any discernible current decay, demonstrating the material's exceptional stability. Figure 6c displays cyclic voltammograms (CVs) of Au-NiS@rGO and NiS. When considering the entire potential range, the total number of active sites correlates with the integrating charge [36]. Active site densities are expected to be  $1.49 \times 10^{16} \text{ cm}^{-2}$  for NiS and  $1.85 \times 10^{16} \text{ cm}^{-2}$  for Au-NiS@rGO nanohybrids. As a result, the enhanced number of active sites may speed up either the Volmer step or the dissociation of water. More active edge sites can be made available for HER because of the accumulation of Au-NiS NPs on the rGOs, as shown by the increased density of active sites [37]. Table 1 also includes the HER parameters. The results of this study's HER activity are described in Table 2, which shows that they are significantly higher than those found in previously reported studies [38–46]. Photocurrent responses have long been used as evidence that charge transfer and dissociation play important roles in determining catalytic activity during photocatalysis. Under visible light irradiation, Fig. 7a displays the photocurrent responses of NiS, NiS@rGO,

**Fig. 6** **a** The polarization curves of the Au/NiS@rGO recorded initially and after 5000 CV cycles. **b** Chronopotentiometry curve of the Au/NiS@rGO at an overpotential of 260 mV (vs. RHE) for 98 h. **c** CV curves of NiS and Au/NiS@rGO. In phosphate-buffered solution (pH 7) with scan rates of  $50 \text{ mVs}^{-1}$  in the potential ranging from  $-0.8$  to  $0 \text{ V}$  vs. SCE, **(d)** TOF Curves of NiS and Au/NiS@rGO

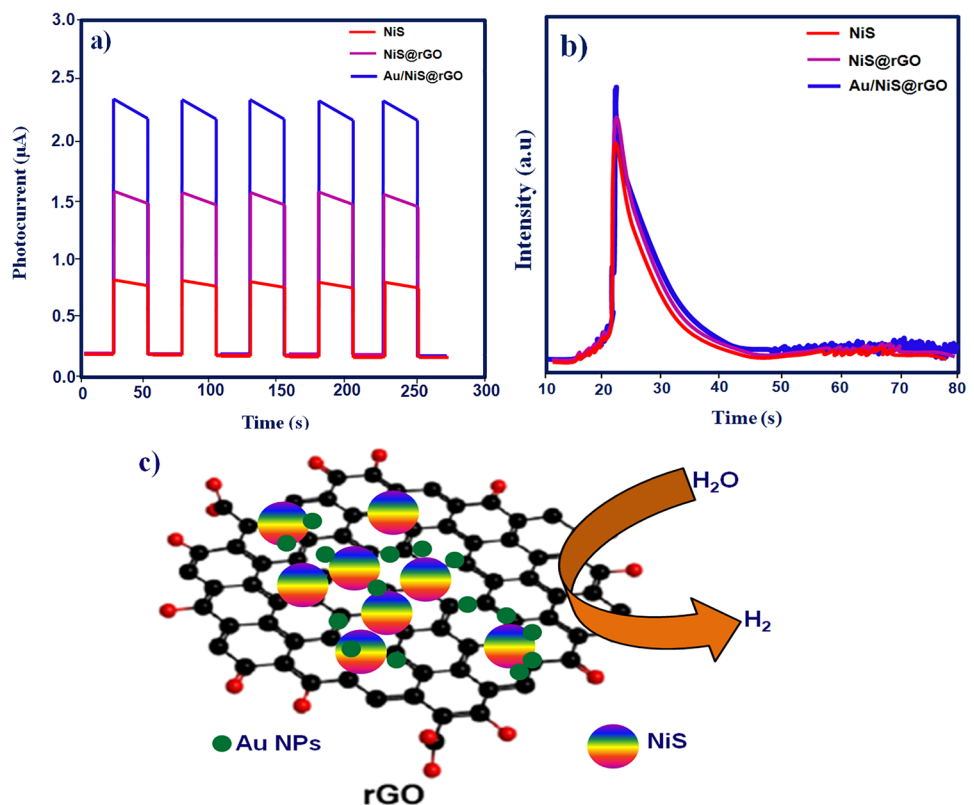


**Table 1** HER parameters of Au NPs-loaded NiS@rGO composite

Sample	Onset (mV)	$\eta/mV$ ( $i = 10 \text{ mA cm}^{-2}$ )	Tafel slope ( $mV \text{ Dec}^{-1}$ )	$j_0 = (\text{mA cm}^{-2})$	ECSA ( $\text{cm}^2$ )
NiS	167	232	64	$1.3E^{-3}$	467
NiS@rGO	161	215	58	$2.7 E^{-3}$	1165
Au/NiS@rGO	252	198	54	$3.9 E^{-3}$	1876

**Table 2** Comparison performance of HER activity between this work and already published works

Catalyst	Electrolyte	Overpotential at $10 \text{ mA cm}^{-2}$ (mV vs. RHE)	Tafel slope ( $mV \text{ dec}^{-1}$ )	References
CuS-Au	0.5 M $\text{H}_2\text{SO}_4$	167	75	[38]
3D $\text{MoS}_2$ -rGO@Mo	0.5 M $\text{H}_2\text{SO}_4$	128	64	[39]
Fe-NiS/NiS <sub>2</sub>	1.0 M $\text{H}_2\text{SO}_4$	179	61	[40]
NiS/Ni <sub>2</sub> P	1.0 M KOH	121	98	[41]
CoS/NiS@CuS	0.5 M $\text{H}_2\text{SO}_4$	190	89	[42]
$\alpha$ -NiS/CdS p-n	1.0 M KOH	121	92	[43]
NiS/ CdS/MIL-101	0.5 M $\text{H}_2\text{SO}_4$	190	89	[44]
Mo-NiS@NiTe	1.0 M KOH	34	57	[45]
NiS@CuBi <sub>2</sub> O <sub>4</sub> /ERGO	1.0 M KOH	210	76	[46]
Au/NiS@rGO	0.5 M $\text{H}_2\text{SO}_4$	252	54	This work

**Fig. 7** **a** Photocurrent responses of NiS, NiS@rGO, and Au-NiS@rGO samples under visible light irradiation. **b** Time decay profile of NiS, NiS@rGO, and Au-NiS@rGO samples. **c** Schematic representation of the HER performance of Au NPs-loaded NiS@rGO composite

and Au-NiS@rGO. Recombination of photo-induced electron-hole pairs is evidenced by a rapid decay of the photocurrent to zero when the light source is turned off. All samples show transitory photocurrent responses that are reversible and rather constant in the presence and absence of illumination. With a greater photocurrent, Au-NiS@rGO hybrid photocatalysts exhibit a more effective charge transfer process and a longer lifespan of electron-hole pairs as opposed to pure NiS. To further confirm the charge transfer process, dependent on time, photoluminescence spectra were also investigated. As can be seen in Fig. 7b, the PL decay kinetics of the Ag/NiS@rGO heterostructures is faster than that of bare NiS (averaged time constant, 12.45 ps). Large contact areas between NiS and rGO were responsible for the efficient extinction, which led to the quicker decay. High electron conductivity via the carbon network (Fig. 7c) and the Schottky barrier at the metal-metal interface (Fig. 7b) may be responsible for the improved photocatalytic activity of H<sub>2</sub> evolution. The nanocomposite's ability to absorb visible light is enhanced by the special properties of Au nanoparticles, such as SPR. Excited to their surface plasmon state by absorbed photon energy, plasmonic metals generate an electric field in their immediate vicinity. This initiates the HER reaction by driving an electron to the semiconductor surface via a carbon-based support. To further boost overall electrocatalytic efficiency toward the hydrogen evolution reaction, Au doping has also formed flaws in NiS planes, which may have activated unsaturated active sites as indicated above.

## 4 Conclusion

In conclusion, a hybrid composite photocatalyst of Au-loaded NiS/rGO has been demonstrated to have excellent HER performance. Because of the SPR impact and the space confinement effect among the rGO layer, the loaded Ag and rGO successfully stifled the expansion of the NiS nanostructure. Excellent HER activity was shown by the porous Au-NiS/rGO nanohybrids in an alkaline solution, with a tiny overpotential of 252 mV at a current density of 10 mAcm<sup>-2</sup> and a small Tafel slope of 54 mV dec<sup>-1</sup>. Together, the 2D nanostructure, the high electrical conductivity, and the abundance of active sites contributed to the increased HER activity. One possible use for these nanohybrids is as a catalyst for the efficient splitting of water into hydrogen and oxygen. Three factors contribute to the enhanced

HER activity: (1) the abundant heterogeneous connection between NiS and rGO can expose dense catalytic locations and increase electron transfer, synergistically promoting electrocatalytic activity in a broad pH range; (2) the increased interlayer distance of NiS reveals more insignificant active edge sites; and (3) the high inherent electrical conductivity of rGO allows the rate of charges transfer among electrode and active catalytic site.

## Author contributions

PS and AS contributed toward study conceptualization and writing (original draft) the manuscript. KP and SPS, contributed toward data curation, formal analysis, and writing (review and editing).

## Data availability

The data that support the findings of this study are available from the corresponding author, upon reasonable request.

## Declarations

**Conflict of interest** The authors declare that there is no conflict of interest regarding the research work reported in this manuscript.

**Supplementary Information** The online version contains supplementary material available at <https://doi.org/10.1007/s10854-023-11684-0>.

## References

1. Z. Heydariyan, R. Monsef, E.A. Dawi, M. Salavati-Niasari, EuMnO<sub>3</sub>/EuMn<sub>2</sub>O<sub>5</sub>/MWCNT nanocomposites: Insights into synthesis and application as potential materials for development of hydrogen storage capacity. *Fuel* **1**(351), 128885 (2023)
2. A. Karami, R. Monsef, I. Waleed, H.L. Kareem, I.T. Ibrahim, M. Salavati-Niasari, Microwave synthesized erbium vanadate nano-photocatalyst: application for enhanced degradation of contaminated water. *Int. J. Hydrogen Energy* **48**(23), 8499–8513 (2023)

3. M. Salavati-Niasari, F. Davar, Shape selective hydrothermal synthesis of tin sulfide nanoflowers based on nanosheets in the presence of thioglycolic acid. *J. Alloys Compds.* **492**(1–2), 570–575 (2010)
4. A.M. Abdalla, S. Hossain, O.B. Nis, A.T. Azad, Hydrogen production, storage, transportation and key challenges with applications: a review. *Energy Convers. Manag.* **165**, 602–627 (2018)
5. N. Rakesh, S. Dasappa, Analysis of tar obtained from hydrogen-rich syngas generated from a fixed bed down-draft biomass gasification system. *Energy Convers. Manag.* **167**, 134–146 (2018)
6. Q. Wang, Y. Zhao, Z. Zhang, S. Liao, Y. Deng, X. Wang, Q. Ye, K. Wang, Hydrothermal preparation of  $\text{Sn}_3\text{O}_4/\text{TiO}_2$  nanotube arrays as effective photocatalysts for boosting photocatalytic dye degradation and hydrogen production. *Ceram. Int.* **49**, 5977–5985 (2023)
7. Y.-C. Chang, S.-Y. Syu, Wu, Zi-Ying, Fabrication of  $\text{ZnO-In}_2\text{S}_3$  composite nanofiber as highly efficient hydrogen evolution photocatalyst. *Mater. Lett.* **302**, 130435 (2021)
8. Z. Ashfaq, T. Iqbal, H. Ali, S.M. Eldin, F.F. Al-Harbi, M. Arshad, A.M. Galal, Review of different  $\text{CdS}/\text{TiO}_2$  and  $\text{WO}_3/\text{g-C}_3\text{N}_4$  composite based photocatalyst for hydrogen production. *Arab. J. Chem.* **30**, 105024 (2023)
9. S.Y. Tee, K.Y. Win, W.S. Teo, L.D. Koh, S. Liu, C.P. Teng, M.Y. Han, Recent progress in energy-driven water splitting. *Adv. Sci.* **4**, 1600337 (2017)
10. K. Fujishima, Honda, Electrochemical photolysis of water at a semiconductor electrode. *Nature* **238**, 37–38 (1972)
11. W.L. Silva, A.L. Marla, Síntese, caracterização e atividade fotocatalítica de catalisadores nanoestruturados de  $\text{TiO}_2$  dopados com metais. *Quím* **36**, 382–386 (2013)
12. L. Jiang, X. Yuan, Y. Pan, J. Liang, G. Zeng, Z. Wu, H. Wang, Doping of graphitic carbon nitride for photocatalysis: a review. *Appl. Catal. B Environ.* **217**, 388–406 (2017)
13. H. Tong, S. Ouyang, Y. Bi, N. Umezawa, M. Oshikiri, J. Ye, Nano-photocatalytic materials: possibilities and challenges. *Adv. Mater.* **24**, 229–251 (2012)
14. K. Woan, G. Pyrgiotakis, W. Sigmund, Photocatalytic carbon-nanotube- $\text{TiO}_2$  composites. *Adv. Mater.* **21**, 2233–2239 (2009)
15. S.K. Cushing, J. Li, F. Meng, T.R. Senty, S. Suri, M. Zhi, M. Li, A.D. Bristow, N. Wu, Photocatalytic activity enhanced by plasmonic resonant energy transfer from metal to semiconductor. *J. Am. Chem. Soc.* **134**, 15033–15041 (2012)
16. J. Zhou, F. Ren, S. Zhang, W. Wu, X. Xiao, Y. Liu, C. Jiang,  $\text{SiO}_2\text{-Ag-SiO}_2\text{-TiO}_2$  multi-shell structures: plasmon enhanced photocatalysts with wide-spectral response. *J. Mater. Chem.* **1**, 13128–13138 (2013)
17. L. Wang, L. Zan, Band-gap-energy-adjustable and noble-metal-free modified  $\text{NiS-Zn}_x\text{Cd}_{1-x}\text{S}$  for highly efficient visible-light-driven  $\text{Cr}^{6+}$  photoreduction in alkaline wastewater. *J. Phys. Chem. Solids* **150**, 109893 (2021)
18. D.M. Muir, E. Ho, Process review and electrochemistry of nickel sulphides and nickel mattes in acidic sulphate and chloride media. *Miner. Process. Extr. Metall.* **115**, 57–65 (2013)
19. K. He, L.J. Guo, Highly efficient and stable photocatalysts for hydrogen production from water. *Int. J. Hydrogen Energy* **42**, 23995 (2017)
20. K.T. Alali, Z. Lu, H. Zhang, J. Liu, Q. Liu, R. Li, K. Aljebawi, J. Wang, P-p heterojunction  $\text{CuO}/\text{CuCo}_2\text{O}_4$  nanotubes synthesized via electrospinning technology for detecting n-propanol gas at room temperature. *Inorg. Chem. Front.* **4**(7), 1219–30 (2017)
21. M. Zhou, D. Han, X. Liu, C. Ma, H. Wang, Y. Tang et al., Enhanced visible light photocatalytic activity of alkaline earth metal ions-doped  $\text{CdSe}/\text{rGO}$  photocatalysts synthesized by hydrothermal method. *Appl Catal B* **172**, 174–184 (2015)
22. H. Zhang, X.J. Lv, Y.M. Li, Y. Wang, J.H. Li,  $\text{P25-graphene}$  composite as a high performance photocatalyst. *ACS Nano* **4**, 380–386 (2010)
23. C. Xu, X. Wang, J.W. Zhu, Graphene—metal particle nanocomposites. *J. Phys. Chem. C* **112**, 19841 (2008)
24. S. Stankovich, D.A. Dikin, R.D. Piner, K.A. Kohlhaas, A. Kleinhammes, Y. Jia et al., Synthesis of graphene-based nanosheets via chemical reduction of exfoliated graphite oxide. *Carbon* **45**, 1558–1565 (2007)
25. M.S. Dresselhaus, A. Jorio, M. Hofmann, G. Dresselhaus, R. Saito, Perspectives on carbon nanotubes and graphene Raman spectroscopy. *Nano Lett.* **10**, 751–758 (2010)
26. J. Hong, Y. Wang, Y. Wang, W. Zhang, R. Xu, Noble-metal-free  $\text{NiS}/\text{C}_3\text{N}_4$  for efficient photocatalytic hydrogen evolution from water. *Chemsuschem* **6**, 2263–2268 (2013)
27. Z. Chen, P. Sun, B. Fan, Z. Zhang, X. Fang, In situ template-free ion-exchange process to prepare visible-light-active  $\text{g-C}_3\text{N}_4/\text{NiS}$  hybrid photocatalysts with enhanced hydrogen evolution activity. *J. Phys. Chem. C* **118**, 7801–7807 (2014)
28. Q. Lin, L. Li, S. Liang, M. Liu, J. Bi, L. Wu, Efficient synthesis of monolayer carbon nitride 2D nanosheet with tunable concentration and enhanced visible-light photocatalytic activities. *Appl. Catal. B* **163**, 135–142 (2015)
29. S. Kai, B. Xi, X. Liu, Ju. Lin, P. Wang, Z. Feng, X. Ma, S. Xiong, An innovative  $\text{Au-CdS}/\text{ZnS-RGO}$  architecture for efficiently photocatalytic hydrogen evolution. *J. Mater. Chem. A* **6**, 895–2899 (2018)

30. M. Jayashree, V. Sharmila, K.L. Meganathan, R. Boopathi Raja, M. Parthibavarman, M. Shkir, S. AlFaify, Design and fabrication of graphene anchored CeO<sub>2</sub> hybrid nanocomposite electrodes for high performance energy storage device applications. *Inorg. Chem. Commun.* **132**, 108838 (2021)
31. R. BoopathiRaja, M. Parthibavarman, Hetero-structure arrays of MnCo<sub>2</sub>O<sub>4</sub> nanoflakes@ nanowires grown on Ni foam: design, fabrication and applications in electrochemical energy storage. *J. Alloy Compd.* **811**, 152084 (2019)
32. R. Boopathi Raja, M. Parthibavarman, A. Nishara Begum, Hydrothermal induced novel CuCo<sub>2</sub>O<sub>4</sub> electrode for high performance supercapacitor applications. *Vacuum* **165**, 96–104 (2019)
33. M.P. Seah, I.S. Gilmore, G. Beamson, XPS: binding energy calibration of electron spectrometers 5-re-evaluation of the reference energies. *Surf. Interface Anal.* **26**, 642–649 (1998)
34. S. Yan, Y. Shi, L. Sun, Z. Xiao, B. Sun, X. Xu, Controlled synthesis of NiS nanoparticle/CdS nanowire heterostructures via solution route and their optical properties. *Mater. Sci. Eng. B* **178**, 109–116 (2013)
35. Y. You, Y. Ye, M. Wei, W. Sun, Q. Tang, J. Zhang, X. Chen, H. Li, J. Xu, Three dimensional MoS<sub>2</sub>/rGO foams as efficient sulfur hosts for high-performance lithium-sulfur batteries. *Chem. Eng. J.* **355**, 671–678 (2019)
36. D. Merki, S. Fierro, H. Vrubel, X. Hu, Amorphous molybdenum sulfide films as catalysts for electrochemical hydrogen production in water. *Chem. Sci.* **2**, 1262–1267 (2011)
37. T. Hu, K. Bian, G.A. Tai, T. Zeng, X. Wang, X. Huang, K. Xiong, K. Zhu, Oxidation-sulfidation approach for vertically growing MoS<sub>2</sub> nanofilms catalysts on molybdenum foils as efficient HER catalysts. *J. Phys. Chem. C* **120**, 25843–25850 (2016)
38. M. Basu, R. Nazir, P. Fageria, S. Pande, Construction of CuS/Au heterostructure through a simple photoreduction route for enhanced electrochemical hydrogen evolution and photocatalysis. *Sci. Rep.* **6**, 34738 (2016)
39. B. He, L. Chen, M. Jing, M. Zhou, Z. Hou, X. Chen, 3D MoS<sub>2</sub>-rGO@Mo nanohybrids for enhanced hydrogen evolution: The importance of the synergy on the Volmer reaction. *Electrochim. Acta* **283**, 357–365 (2018)
40. X. Zhao, X. Wang, L. Chen, X. Kong, Z. Li, Y. Zhao, T. Wang et al., The design and synthesis of Fe doped flower-like NiS/NiS<sub>2</sub> catalyst with enhanced oxygen evolution reaction. *J. Electroanal. Chem.* **920**, 116630 (2022)
41. Y. Huang, Y. Pan, X. Huang, J. Zhao, X. Wang, Porous NiS@Ni<sub>2</sub>P nanoframe as a multi-functional catalyst for enhanced oxygen evolution and urea oxidation reactions. *J. Ind. Eng. Chem.* **118**, 239–246 (2023)
42. Q. Wang, Du, Xiaoqiang, X. Zhang, Construction of CoS/NiS@CuS with dandelion flower-like heterostructures as efficient catalysts for overall urea splitting. *Int. J. Hydrogen Energy* **48**, 24342–24355 (2023)
43. X. Fan, B. Wang, Q. Heng, W. Chen, L. Mao, Facile in-situ synthesis of α-NiS/CdS p-n junction with enhanced photocatalytic H<sub>2</sub> production activity. *Int. J. Hydrogen Energy* **47**, 32531–32542 (2022)
44. H. Chang, W. Fan, J. Liu, Z. Jiang, Y. Li, Y. Zhang, J. Zhang, Polyoxo-titanium clusters promoted photocatalytic H<sub>2</sub> evolution activity in a NiS modified CdS/MIL-101 system. *Int. J. Hydrogen Energy* **46**, 6369–6379 (2021)
45. Ke. Zhang, E. Yang, Y. Zheng, Yu. Dehua, J. Chen, Y. Lou, robust and hydrophilic Mo-NiS@NiTe core-shell heterostructure nanorod arrays for efficient hydrogen evolution reaction in alkaline freshwater and seawater. *Appl. Surf. Sci.* **637**, 157977 (2023)
46. H.Ö. Doğan, B.K. Urhan, NiS@CuBi<sub>2</sub>O<sub>4</sub>/ERGO heterostructured electro-catalyst for enhanced hydrogen evolution reaction. *Micro Nanostruct.* **183**, 207666 (2023)

**Publisher's Note** Springer Nature remains neutral with regard to jurisdictional claims in published maps and institutional affiliations.

Springer Nature or its licensor (e.g. a society or other partner) holds exclusive rights to this article under a publishing agreement with the author(s) or other rightsholder(s); author self-archiving of the accepted manuscript version of this article is solely governed by the terms of such publishing agreement and applicable law.